ELSEVIER

Sensors and Actuators A 57 (1996) 103–110

SENSORS AND ACTUATORS A PHYSICAL

Laminated high-aspect-ratio microstructures in a conventional CMOS process

G.K. Fedder [a,b], S. Santhanam [a], M.L. Reed [a], S.C. Eagle [a], D.F. Guillou [a], M.S.-C. Lu [a], L.R. Carley [a]

[a] *Department of Electrical and Computer Engineering, Carnegie Mellon University, Pittsburgh, PA 15213-3890, USA*
[b] *The Robotics Institute, Carnegie Mellon University, Pittsburgh, PA 15213-3890, USA*

Abstract

Electrostatically actuated microstructures with high-aspect-ratio laminated-beam suspensions have been fabricated using a 0.8 μm three-metal CMOS process followed by a sequence of three maskless dry-etching steps. Laminated structures are etched out of the CMOS silicon oxide, silicon nitride, and aluminum layers. The key to the process is the use of the CMOS metallization as an etch-resistant mask to define the microstructures. A minimum beam width of 1.2 μm, gap of 1.2 μm, and maximum beam thickness of 4.8 μm are obtained. These structural features will scale in size as the CMOS technology improves. The laminated material has an effective Young's modulus of 61 GPa, an effective residual stress of 69 MPa, and a residual strain gradient of 2×10^{-4} μm^{-1}. Multi-conductor electrostatic micromechanisms, such as self-actuating springs, *x–y* microstages, and nested comb-drive lateral resonators, are successfully produced. A self-actuating spring is a lateral electrostatic microactuator without a stator that is insensitive to out-of-plane curl. A spring 107 μm wide by 109 μm long excited by an 11 V a.c. signal has a measured resonance amplitude of 1 μm at 14.9 kHz. Finite-element simulation using the extracted value for Young's modulus predicts the resonance frequencies of the springs to within 7% of the measured values.

Keywords: CMOS process; High-aspect-ratio microstructures

1. Introduction

Microstructures integrated with CMOS are commonly made from combinations of aluminum, silicon oxide, and silicon nitride thin films by undercutting the silicon substrate, which acts as the sacrificial material [1]. The metallization and dielectric layers, normally used for electrical interconnect, now serve a dual function as structural layers. Microstructures compatible with CMOS processes have also been made using the gate polysilicon as the structural layer and field oxide as the sacrificial material [2]. There are many advantages to leveraging conventional CMOS processing for microelectromechanical systems (MEMS). Fabrication is fast, reliable, repeatable, economical, and available through external foundries. Integrated MEMS capabilities, built into the process, will improve with the scaling of CMOS technology. One of the limitations of post-processed CMOS microstructures has been an inability to create microstructures with narrow beam widths and narrow gaps for lateral electrostatic actuation and capacitive sensing. To date, lateral electrostatic microstructures have been primarily produced using polysilicon surface micromachining. In this paper, a simple maskless post-CMOS process capable of producing beam widths and gaps down to 1.2 μm is introduced. New lateral electrostatic actuator designs are possible using this process.

A comparison of the previous and new CMOS microstructural processes is first presented, followed by a discussion of design issues, and characterization of some example devices that take advantage of the unique aspects of this process.

2. Previous processes

Previously, conventional CMOS processing has been used to make thermal flow sensors [3], accelerometers [4], thermally isolated transistors [5], infrared sensors [6], and 3-D assembled structures [7]. Structures have been released by dry etching, wet etching, and electrochemical wet etching of the bulk silicon. The previous work has resulted in static structures for thermal isolation and movable beams and plates having vertical actuation. A series of cross sections is shown in Fig. 1 for a CMOS microstructural process that we initially investigated and that is similar to previous work. By stacking the drain/source contact cut and metal via cuts, the substrate

PII S0924-4247(96)01343-X

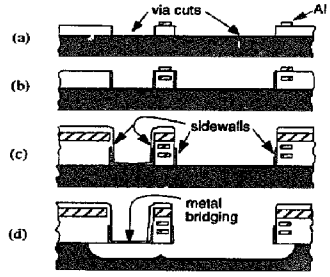

Fig. 1. Cross sections of the stacked-via process. (a) After first metal, showing exposed via cuts. (b) After second metal, showing via stacking. (c) After pad overglass cut; metal/oxide sidewalls are identified. (d) After silicon dry etch to release microstructures; metal bridging is evident in narrow gaps between structures.

is exposed at the end of the CMOS process. Laminated aluminum/oxide microstructures are defined from the stacked via cuts.

Via and metal-etching steps in the foundry process are tailored for planarized interconnect, not for the creation of micromechanical structures. Since the stacked vias are not covered with metal, the layout violates the CMOS design rules, resulting in very non-planar topography and formation of metal and dielectric sidewalls. These sidewall films adversely affect the effective beam width by 1 μm or more. The asymmetric beam cross section produces a large strain gradient in the structure, which causes the beams to curl out of plane. Very narrow lateral gaps cannot be fabricated because of the large topography of the oxide cuts. In past processes where we had used stacked vias, the structure spacing was limited to about 10 μm for acceptable yield. An example of these sidewall and bridging problems for narrow beam spacing is shown in Fig. 2. Incomplete etching of the metal in the oxide-cut regions causes bridging for gaps smaller than about 10 μm. The structural yield is highly dependent on the CMOS vendor and varies from run to run. Other yield problems can arise from polymerization of the silicon and oxide surfaces due to excessive overetching.

Wet-etch release using KOH, ethylenediamine–pyrocatechol (EDP) or tetramethylammonium hydroxide (TMAH) requires careful control of the etchant chemistry to provide uniform silicon etching and to prevent undesired etching of the aluminum. Agitation during etching can cause breakage of very fragile structures, and surface-tension forces during the drying step can lead to sticking. These drawbacks of previous processes motivated us to develop a new CMOS-compatible process that enabled fabrication of lateral electrostatic actuators and that had a dry-etch release.

3. New process

In contrast to structural definition within the CMOS process, structural definition performed after completion of

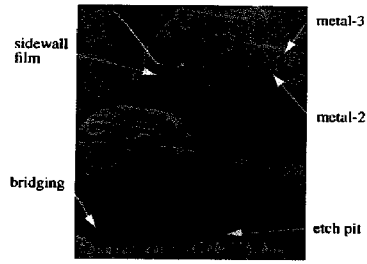

Fig. 2. SEM of two beams fabricated in the stacked-via process. The sidewall profile is uneven and additional sidewall films and bridging are evident in the narrow gaps between the beams.

the CMOS process can be optimized for etching of high-aspect-ratio beam suspensions and narrow-gap electrostatic actuators. The top metal interconnect layer is used as an etch-resistant mask for the microstructure definition. A series of dry etches creates the microstructures and releases them from the substrate.

The key feature of the new process is that minimum beam widths and gaps are set by the CMOS design rules and scale with the CMOS technology. However, as with the stacked-via microstructural process, the mechanical properties of the resulting thin-film laminated structures are dependent on the CMOS vendor. A manufacturable process must control such thin-film mechanical properties as residual stress, stress gradient, and Young's modulus.

Structures are made using the Hewlett-Packard 0.8 μm three-metal n-well CMOS process available through the MOS Implementation Service (MOSIS). The process flow in Fig. 3 shows the development of a high-aspect-ratio beam in cross section [8]. The dice which come back from MOSIS have CMOS circuits covered by the metal-3 and oxide layers as shown in Fig. 3(a). The top metal layer is used as the etch-resistant mask during the subsequent dry etching that creates the laminated microstructures. Oxide areas not covered by

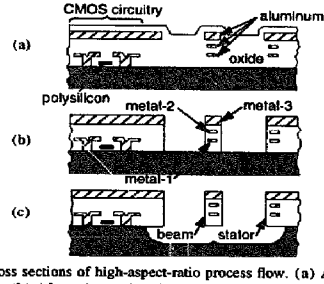

Fig. 3. Cross sections of high-aspect-ratio process flow. (a) After CMOS processing. (b) After anisotropic oxide etch. (c) After silicon etch for beam release.

Table 1
Post-CMOS dry-etch steps

	(1) Inter-metal oxide etch	(2) Field oxide etch	(3) Si etch for release
Gas flow [sccm]	47 CHF_3, 4.5 O_2	47 CHF_3, 3 O_2	50 SF_6, 10 O_2
Pressure [mtorr]	50	25	100
Power [W]	100	50	60
Etch rate [Å min^{-1}]	360	125	5000

metal are anisotropically etched in a two-step CHF_3/O_2 reactive ion etch (RIE) for 120 min, resulting in cross section (b). In (c), a final SF_6/O_2 low-power silicon etch releases the structure with a minimum amount of non-uniformity across the die and a controllable underlying surface roughness. In contrast to wet-etch release, the dry-etch release process prevents breakage and sticking of structures to the substrate and to each other.

A scanning electron micrograph (SEM) of a released microstructure in shown in Fig. 4(a). The corresponding schematic (Fig. 4(b)) gives approximate dimensions of the laminated structure. Layout of the metal layers was deliberately overlapped to produce the sidewall stair-step pattern and highlight the various layers. (A conventional, stacked metal-1/metal-2/metal-3 via produces the indentation at the top of the structure.) The dielectric between metal layers is a laminate of approximately 0.5 μm thick oxide and nitride films. If desired, the gate polysilicon layer can be added to the laminated beam, providing an extra electrical interconnect inside the structure.

The dry-etch steps take place in a Plasma-Therm 790 reactor and are summarized in Table 1 with the operating parameters. The two-step oxide RIE (steps 1 and 2 in Table 1) is designed to etch cleanly through the thick oxide layers, while maximizing selectivity to aluminum. In regions where the metal-3 layer exists, the two-step oxide RIE removes the overglass and mills off about 0.25 μm of the aluminum. The tapered sidewall on metal-3 (Fig. 4(a)) is due to preferential ion milling at about a 60° angle. Excessive aluminum milling causes metal-3 to metal-2 vias to fail first at the beveled edge. The etch power is made as small as possible to minimize erosion of the aluminum without reducing the oxide etch rate to an intolerable level. A relatively high pressure of 50 mtorr is used in the first oxide-etch step to lower the d.c. bias and thereby further reduce the aluminum milling. Etching continues until the CMOS field oxide is exposed. However, further etching into the field oxide with this recipe will create oxide 'stringers' at the base of the sidewall. The failure to etch the field oxide properly is believed to be caused by a build-up of passivating film. Square holes smaller than 3.2 μm could not be etched completely, thereby inhibiting the Si release of perforated plates. To solve these problems, a low-power low-pressure recipe (50 W, 25 mtorr) is used to complete the field oxide etch. The two-step oxide-etch sequence defines very clean microstructures with no stringers.

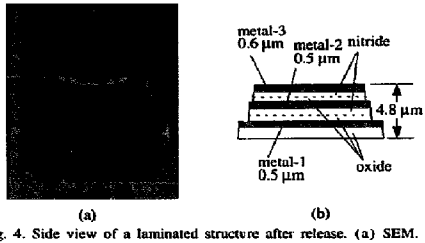

Fig. 4. Side view of a laminated structure after release. (a) SEM. (b) Schematic cross section with approximate film thicknesses.

During the silicon etch for microstructure release (step 3 of Table 1), O_2 is introduced to reduce the lateral oxide etch rate to near zero. A balance must be struck between structural oxide etching and the underlying Si roughness. The current recipe uses reduced power and O_2 flow, resulting in a vertical-to-lateral Si etch rate of approximately 2:1. A benefit of the reduction in power is that a negligible amount of aluminum is milled off the microstructures in this step. Other silicon-etch chemistries, such as XeF_2, have been reported to alleviate the problem of aluminum etching [9].

A corner of a lateral comb-drive microresonator is shown in Fig. 5 after the final release etch. Fine features usually associated with polysilicon micromechanics [10], such as interdigitated comb fingers and compliant meander springs, are made from the laminated structural material. The beams in the Figure are 2.4 μm wide and 4.8 μm thick with gaps down to 1.6 μm between structures. The Si ridges under the suspended structure are a result of the 2:1 vertical-to-lateral silicon etch ratio.

An older process included a highly anisotropic pre-release RIE of the exposed substrate after the oxide etch at 50 sccm SF_6/12.5 sccm O_2 gas flows, 150 mtorr pressure, and 100 W power [11]. The etching characteristics are sensitive to silicon loading in the reactor, so dummy silicon wafers were added. The original purpose of the anisotropic silicon etch was to prevent premature microstructure release, in which the released beams might curl up and the oxide sidewalls might be attacked by the RIE. However this extra etch step was found to be unnecessary in successfully releasing the microstructures.

Preliminary electrical measurements of circuits before and after the structural release indicate that the electronics survive the long RIE steps with no adverse effects. However, full characterization of transistors must be completed to determine any measurable changes in transistor parameters.

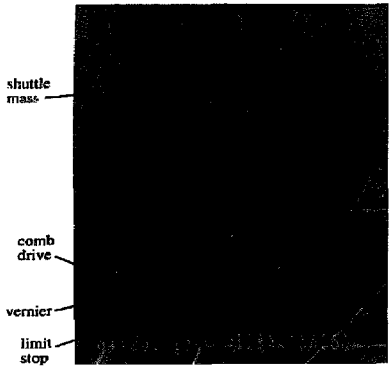

Fig. 5. SEM of a section of a lateral comb-drive microresonator after the isotropic silicon release etch. Several features of the microresonator are identified.

4. Microstructure design rules and characterization

Minimum beam widths and gaps in the new process are set by the CMOS design rules. The scaling factor for the HP 0.8 μm process is $\lambda = 0.4$ μm. The minimum beam width for metal-3 lines is limited to 5λ (2.0 μm). Beams need not be made with all three metal layers. Thinner, more compliant beams can be made by omitting the metal-3 and using either metal-1 or metal-2 as the top mask layer. These thinner beams are limited to 3λ (1.2 μm) width. The minimum gap between structures is also 3λ. Plates must be perforated with evenly spaced holes at most 16 μm apart for release.

The substrate will be etched anywhere a metal layer is not present. A sheet of metal-3 is used to cover all regions containing active MOS devices or other electronic components. However, a gap in metal-3 is necessary for electrical isolation between external pads and the rest of the metal-3 plane. The interconnect arrangement is shown in Fig. 6. A metal-1 or metal-2 collar is inserted underneath the break in metal-3 to prevent the silicon etch from reaching the substrate surface. Such gaps in metal are also used to isolate electrically different conducting areas on suspended structures.

Resonance-frequency values of three cantilever beams were measured optically to extract a preliminary value for an effective Young's modulus. The beams were excited by lateral electrostatic actuators placed near the tips. Resonance-

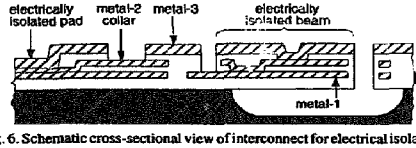

Fig. 6. Schematic cross-sectional view of interconnect for electrical isolation.

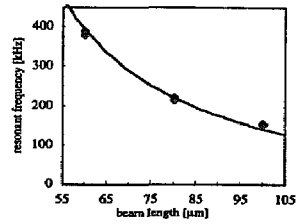

Fig. 7. Resonance frequency vs. cantilever beam length. Points are measured values, the solid line is an analytic best fit using 61 GPa as the effective Young's modulus.

frequency values are plotted as a function of beam length in Fig. 7. The data are fitted with the analytic equation for resonance frequency of a homogeneous beam,

$$f_r = 0.56\sqrt{\frac{EI}{mL^4}} \tag{1}$$

where L is the beam length, EI is the effective lateral beam stiffness, and m is the mass per unit length. The beams are of width 1.2 μm, height 4.8 μm, and have lengths of 60, 80, and 100 μm. An effective stiffness value of 1.45×10^{-13} N m^2 gives a least-squares fit to the data, where the densities of the aluminum, oxide, and nitride films are assumed to be 2700, 2500, and 3100 kg m^{-3}, respectively. The stiffness corresponds to an effective Young's modulus of 61 GPa.

Residual stress was measured using bent-beam strain test structures [12]. The 3-metal laminated material has a lateral residual stress of 69 MPa, corresponding to a strain of 1.1×10^{-3}. The buckling length for a 1.2 μm wide fixed–fixed beam is 65 μm. Curling of the structural material arises from the residual vertical strain gradient in the laminated structures. The measured tip displacement of several 1.4 mm long, 3.6 μm wide, 4.8 μm thick beams is 200 ± 30 μm, which corresponds to a nominal radius of curvature of 4.9 mm and a strain gradient of 2×10^{-4} μm^{-1}. Beams made from other laminated combinations of layers have different values of strain gradient.

5. Electrostatic actuator designs

Several different electrostatic actuator designs have been implemented in the new laminated microstructure process. Three new designs are described: the self-actuating spring, the stator meander actuator, and the nested comb-finger actuator. These actuators are constructed by taking advantage of the multiple conductors embedded within a single beam. In contrast, microstructures made from a homogeneous conductive material, such as polysilicon, are restricted to application of a single voltage on the movable structure.

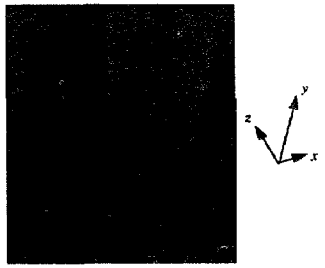

Fig. 8. SEM of a self-actuating spring test structure with 22 meanders. The spring compresses in the y direction with applied voltage. A vernier, shown near the bottom of the micrograph, is used to measure position.

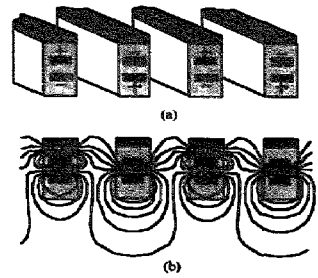

Fig. 9. (a) Internal conductor configuration for the self-actuating spring of Fig. 8. Light gray conductors are grounded and black conductors are set to a positive potential. (b) Equipotential plot.

5.1. Self-actuating spring

One example of multi-conductor electrostatic actuation is the self-actuating spring shown in Fig. 8. The meander beams in the spring are 93 μm long and have the cross section shown in Fig. 9(a). The metal-1 and metal-2 conductors embedded in the beam alternate polarity through via connections at the end of each meander segment. In this design, the metal-3 electrode is grounded. By applying a voltage across the embedded conductors, the dipole pattern shown in Fig. 9(b) is formed, which produces an attractive electrostatic force. The distributed force along each meander compresses the spring. Electrostatic finite-element simulation gives a distributed force of 0.63 μN m^{-1} V^{-2} along each meander.

Electrostatic actuators that require a stator structure are restricted to a maximum displacement equal to the gap between the stator and rotor. In contrast, the self-actuating spring does not have this restriction and is free to compress with a large displacement. Similar piezoresistive self-actuating springs made from quartz have been reported previously [13]. The self-actuating spring in Fig. 8 is curled out of the substrate plane by about 4 μm at the tip. However, since the distributed actuation mechanism is self-aligned throughout the spring structure, the curling does not significantly reduce the electrostatic force.

In resonant operation, the lowest excited mode of the spring is the in the y direction, which is the third eigenmode. (The first and second modes are in the x and z directions, respectively.) Higher-order lateral spring modes are observed at higher excitation frequencies. Measured and simulated resonance-frequency values are given in Table 2 for the lowest excited resonance. The finite-element simulation uses the effective Young's modulus value extracted from the cantilever measurements. Cross-section measurements from the cantilever beams are used to predict the sidewall geometry of the self-actuating spring in the simulations. Measured and simulated values match to within 7.6%, demonstrating reasonable accuracy of the effective Young's modulus value in predictive design. The systematic error is attributed to process variations across the wafer and to errors in the geometric cross-section extraction. The quality factor (Q) was measured at atmospheric pressure in air. The damping is dominated by viscous air drag. The larger springs experience more damping and have a lower quality factor.

An 11 V, 14.9 kHz sinusoidal signal applied to the 22-meander spring in air gives a lateral resonant amplitude of 1 μm at the end of the beam. No series d.c. voltage is applied. As expected, the resonance amplitude increases with the square of the applied voltage. The test structures have withstood up to 90 V without experiencing breakdown.

A charging effect is observed in the springs, which lessens the effect of d.c. voltage on the static force. For the self-actuating springs, the time constant is on the order of 1s. It is believed that charge migrates on the sidewall of the oxide and nitride layers, acting to shield the d.c. electric field. A static force can be obtained by chopping the applied voltage with balanced high-frequency square-wave modulation. The force remains constant since it varies as the square of the voltage. A high-frequency source is not necessary; however, modu-

Table 2
Lowest-order resonance frequencies (f_r) of the self-actuating spring test structures. Frequency values from experimental measurements, finite-element simulation, and relative error are given, along with the quality factor (Q) in air

Number of meanders	f_r (measured)	f_r (simulation)	Δf_r	Q
12	27.5 kHz	25.4 kHz	−7.6%	75
22	14.9 kHz	14.0 kHz	−6.0%	65
32	10.3 kHz	9.6 kHz	−6.8%	54

lation at frequencies high above resonance filters out any glitches in force due to slewing between voltage levels.

An x–y stage that incorporates self-actuating springs is shown after the oxide etch in Fig. 10. The stage is suspended by eight self-actuating springs which provide differential x–y actuation of the center beams. The inner springs are nested inside a rigid frame, thereby decoupling the two lateral modes. Conductors in the self-actuating springs are used for actuation and cannot be used as general interconnects. Electrical connections to the inner springs are routed from the anchored substrate through two-metal meander springs. The two-metal springs are thinner and less stiff than the self-actuating springs. It is desirable to make the interconnect springs as compliant as possible to minimize their effect on the overall system spring constant. Perforated plates mounted on two sides of the structure provide parallel-plate electrostatic actuation in the vertical direction. To date, the largest static displacement observed for this kind of x–y stage is ± 4 μm.

5.2. Stator meander actuator

A different electrostatic actuator design, called a stator meander actuator, is shown in Fig. 11. As in the case of the self-actuating spring, the stator meander actuator has a dual function as a suspension and an actuator. Fixed stator beams (stator fingers) are interdigitated between each meander of the spring. The cross-section drawing in Fig. 11(b) shows the internal structure of the stator conductors. By switching the polarity of the stator electrodes, the meander spring can be differentially actuated. The metal-3 conductor on each stator finger is electrically isolated at the base using the technique shown earlier in Fig. 6. The maximum displacement is

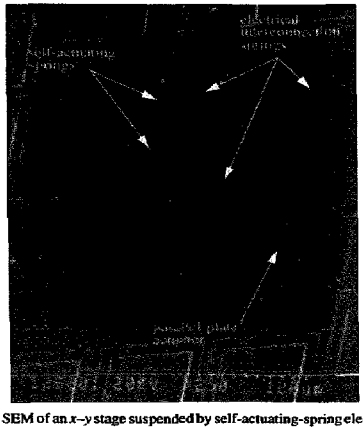

Fig. 10. SEM of an x–y stage suspended by self-actuating-spring electrostatic actuators.

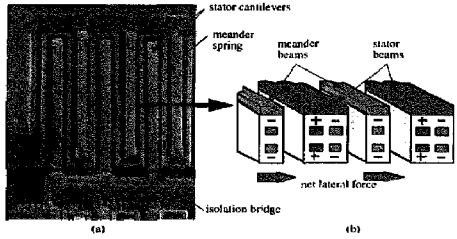

Fig. 11. Stator meander actuator (a) [illegible] a stator meander actuator used in an x–y stage. The individual [illegible]ers are electrically isolated by a metal-2 bridge at the base. (b) Cross-sectional drawing at the cut line shown in (a). Polarity of the inner conductors is indicated, along with the resulting net lateral force acting on the meander spring.

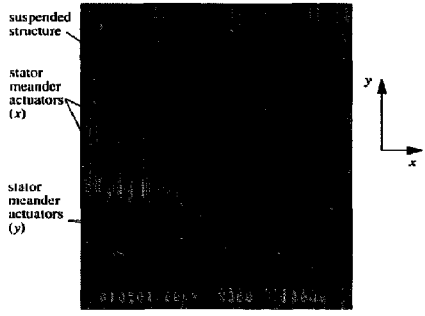

Fig. 12. SEM of an x–y stage suspended by stator meander actuators. Misalignment from curling can be seen in the y-directed actuators (near the top and bottom of the micrograph).

limited by a single gap spacing. The meander spring and stator fingers are not self-aligned. Curling of the stator fingers will cause a misalignment and a corresponding reduction of the lateral electrostatic force for a given voltage.

An x–y microstage using the stator meander actuators is shown in Fig. 12. The suspended structure is a perforated plate with 12 beams sticking out from the plate in the y direction. These beams are not associated with the actuation or suspension of the plate. Eight stator meander actuators are attached to the plate in a two-fold symmetrical arrangement. The symmetry cancels any lateral cross-axis coupling in the individual actuators and ensures that the plate remains flat in the center, independent of residual stress gradients in the structural material.

5.3. Nested comb-finger actuator

Another example of a multi-conductor x–y actuated device is the nested two-axis comb-drive resonator, shown in Fig. 13 after being released from the substrate. The outer frame of the stage is actuated in the x direction by two interdigitated

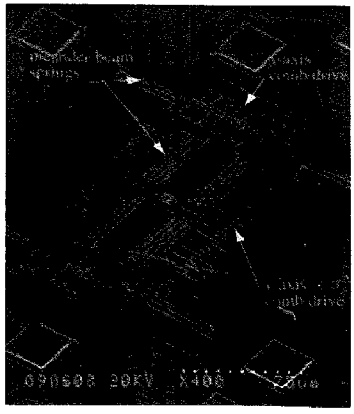

Fig. 13. SEM of a released two-axis nested comb-drive resonator.

comb-finger electrostatic actuators [10]. Independently, the inner section of the stage is actuated in the y direction by a different set of comb drives. The meander-beam suspension does not function as an actuator, so conductors in the beams can be used as interconnects. Wiring is routed through the suspension to provide electrical connections to the inner comb fingers.

6. Conclusions

The simple new method for fabricating high-aspect-ratio microstructures in standard CMOS is an attractive technology with which to make low-cost high-performance integrated sensors and actuators. The dry-release process side-steps the sticking and yield problems associated with competing bulk wet-etch release methods. Beam widths are limited by the minimum allowable metallization linewidths in a given CMOS process. The laminated microstructure process leverages continuing advances in CMOS technology. Microstructures and CMOS devices both scale with the process, enabling subsequent performance improvements in microsensors and microactuators made with this technology.

Multi-conductor laminated microstructures provide additional design flexibility. The conductors can be used for 3-D actuation, sensing, and shielding. However, charging is an issue that must be understood thoroughly before robust microsystems can be designed. Self-aligning lateral microactuators, such as the self-actuating springs, avoid problems with out-of-plane curl.

Acknowledgements

The authors thank Henri Jansen for helping to optimize some of the RIE parameters in our laboratory. The fabrication work was supported in part by the National Science Foundation under grant ECD-8907068. The research effort was sponsored in part by the Advanced Research Projects Agency under the Air Force Office of Scientific Research, Air Force Materiel Command, USAF, under grant number F49620-94-1-0192. The US Government is authorized to reproduce and distribute reprints for Governmental purposes notwithstanding any copyright notation thereon. The views and conclusions contained herein are those of the authors and should not be interpreted as necessarily representing the official policies or endorsements, either expressed or implied, of the Air Force Office of Scientific Research or the US Government.

References

[1] M. Parameswaran, H.P. Baltes, L. Ristic, A.C. Dhaded and A.M. Robinson, A new approach for the fabrication of micromechanical structures, *Sensors and Actuators, 19* (1989) 289–307.

[2] M. Biebl, T. Scheiter, C. Hierold, H.v. Philipsborn and H. Klose, Micromechanics compatible with an 0.8 μm CMOS process, *Sensors and Actuators A, 46–47* (1995) 593–597.

[3] F. Mayer, O. Paul and H. Baltes, Influence of design geometry and packaging on the response of thermal CMOS flow sensors, *Tech. Digest, 8th Int. Conf. Solid-State Sensors and Actuators (Transducers '95)/Eurosensors IX, Stockholm, Sweden, 25–29 June 1995*, Vol. 1, pp. 528–531.

[4] H. Seidel, U. Fritsch, R. Gottinger, J. Schalk, J. Walter and K. Ambaum, A piezoresistive silicon accelerometer with monolithically integrated CMOS-circuitry, *Tech. Digest, 8th Int. Conf. Solid-State Sensors and Actuators (Transducers '95)/Eurosensors IX, Stockholm, Sweden, 25–29 June 1995*, Vol. 1, pp. 597–600.

[5] R.J. Reay, H. Klaasen and G.T.A. Kovacs, Thermally and electrically isolated single crystal silicon structures in CMOS technology, *IEEE Electron Device Lett., 15* (1994) 399–401.

[6] M.J. Syrzycki, L. Carr, G.H. Chapman and M. Parameswaran, A wafer scale visual-to-thermal converter, *IEEE Trans. Compon. Hybrids Manuf. Technol., 16* (1993) 665–673.

[7] E. Hoffman, B. Warneka, E. Kruglick, J. Weigold and K.S.J. Pister, 3D structures with piezoresistive sensors in standard CMOS, *Proc. IEEE Micro Electro Mech. Syst. Workshop, Amsterdam, Netherlands, Jan.–Feb. 1995*, pp. 288–293.

[8] L.R. Carley, M.L. Reed, G.K. Fedder and S. Santhanam, Microelectromechanical structure and process of making same, *US Patent Pending*.

[9] F. I-J. Chang, R. Yeh, G. Lin, P.B. Chu, E. Hoffman, E.J.J. Kruglick and K.S.J. Pister, Gas-phase silicon micromachining with xenon difluoride, *Proc. SPIE, 1995 Symp. Micromachining and Microfabrication, Austin, TX, USA, Oct. 1995*.

[10] W.C. Tang, T.-C.H. Nguyen, M.W. Judy and R.T. Howe, Electrostatic-comb drive of lateral polysilicon resonators, *Sensors and Actuators, A21–A23* (1990) 328–331.

[11] G.K. Fedder, S. Santhanam, M.L. Reed, S.C. Eagle, D.F. Guillou, M.S.-C. Lu and L.R. Carley, Laminated high-aspect-ratio structures in a conventional CMOS process, *Proc. IEEE Micro Electro Mech. Syst. Workshop (MEMS '96), San Diego, CA, USA, Feb. 1996.*, pp. 13–18.

[12] Y.B. Gianchandani and K. Najafi, Bent-beam strain sensors, *J. MEMS, 5* (1996) 52–58.

[13] H. Toshiyoshi, D. Kobayashi, H. Fujita and T. Ueda, A piezoelectric pseudo-static actuator for large displacement under ac voltage operation, *Tech. Digest, 8th Int. Conf. on Solid-State Sensors and Actuators (Transducers '95)/Eurosensors IX, Stockholm, Sweden, 25–29 June 1995*, Vol. 1, pp. 389–392.

Biographies

Gary K. Fedder received the B.S. and M.S. degrees in electrical engineering from Massachusetts Institute of Technology in 1982 and 1984, respectively. In 1994, he received the Ph.D. degree in electrical engineering from the University of California at Berkeley, where his research focused on process development, modeling, and simulation for polysilicon surface microsystems. He joined the faculty of Carnegie Mellon University in October 1994 as an assistant professor holding a joint appointment with the Department of Electrical and Computer Engineering and the Robotics Institute. From 1984 to 1989, he worked at the Hewlett-Packard Company on a VLSI integrated-circuit test system and on modeling of printed-circuit-board interconnect for high-speed computers. He received the 1993 AIME Electronic Materials Society Ross Tucker Award in recognition of his work on MEMS digital multi-mode control. His present research interests include surface-micromachined MEMS in standard CMOS processes, structured design methodologies for MEMS, embedded microsensor packaging, and microrobotics.

Suresh Santhanam received his B.S. in physics from the University of Madras in India and his M.S. in civil engineering from Carnegie Mellon University. He then joined the Data Storage Systems Center as part of its technical staff and is at present the process engineer on the MEMS-based STM-tip data-storage project.

Michael L. Reed received B.S. and M.Eng. degrees in electrical engineering from Rensselaer Polytechnic Institute, and the Ph.D. in electrical engineering from Stanford University. From 1980 to 1983, he was on the staff of Hewlett-Packard Laboratories. Since 1987, he has been on the faculty of Carnegie Mellon University, Department of Electrical and Computer Engineering. He has also held visiting appointments at the University of Twente (Netherlands) and the Swiss Federal Institute of Technology, Zürich. His research interests include microfabrication technology and applications of microelectromechanical systems. Dr Reed was the Technical Co-Chairman of the 1995 IEEE Workshop on MEMS, and the General Co-Chairman of the 1996 Workshop. He is currently serving as an organizer of the MRS Symposium on Materials in Microsystems. He is a recipient of a Hertz Foundation Prize, an IBM Faculty Development Award, and a Presidential Young Investigator Award.

Steven C. Eagle was born in Pennsylvania in 1969. He received a B.S. in electrical engineering with a minor in electronic materials in 1994 and an M.S. in electrical and computer engineering in 1996, both from Carnegie Mellon University in Pittsburgh, PA. He is currently working toward a Ph.D. in electrical and computer engineering at Carnegie Mellon. His research interests include microelectromechanical systems and data-storage techniques. His e-mail address is eagle@henry.ece.cmu.edu.

David F. Guillou is currently pursuing Ph.D. studies in electrical and computer engineering at Carnegie Mellon University. His research interests include analog circuit design for instrumentation and data-storage systems.

Michael S.-C. Lu was born in 1968 in Taipei, Taiwan. He received both his B.S. and M.S. degrees in mechanical engineering from the National Tsing-Hua University, Taiwan, in 1991 and 1993. He is now working toward the Ph.D. degree in the Department of Electrical and Computer Engineering of Carnegie Mellon University.

L. Richard Carley is a professor of electrical and computer engineering at Carnegie Mellon University. He received the S.B. degree from the Massachusetts Institute of Technology in 1976 and was awarded the Guillemin Prize for the best EE Undergraduate Thesis. He remained at MIT, where he received the M.S. degree in 1978 and the Ph.D. in 1984. He has worked for MIT's Lincoln Laboratories and has acted as a consultant in the area of analog circuit design and design automation for Analog Devices, Texas Instruments, Quantum, and Hughes Aircraft among others. In 1984 he joined Carnegie Mellon, and in 1992 he was promoted to full professor. His current research interests include the design of high-performance analog signal-processing ICs, the development of CAD tools to support analog circuit design, the design of low-power high-speed magnetic recording channels, and the design of microelectromechanical systems. He received a National Science Foundation Presidential Young Investigator Award in 1985, a Best Technical Paper Award at the 1987 Design Automation Conference, and a Distinguished Paper Mention at the 1991 International Conference on Computer-Aided Design. He is a senior member of the IEEE.